

Refined numerical modelling for the structural assessment of steel-concrete composite beam-to-column joints under seismic loads



Claudio Amadio^a, Chiara Bedon^{a,*}, Marco Fasan^a, Maria Rosa Pecce^b

^aUniversity of Trieste, Department of Engineering and Architecture, Italy

^bUniversity of Sannio, Department of Engineering, Italy

ARTICLE INFO

Article history:

Received 31 July 2016

Revised 17 November 2016

Accepted 13 February 2017

Keywords:

Steel-concrete composite joints

Seismic loads

Finite-Element numerical modelling

Experimental tests

Design recommendations

Resisting mechanisms

ABSTRACT

This paper proposes a refined Finite-Element (FE) numerical approach to predict both global and local behaviour of steel-concrete composite welded joints subjected to seismic loads. The reference FE model is implemented in ABAQUS and first extensively validated to the full-scale experimental results of a welded steel-concrete composite specimen tested in a past research project, where the beam-to-column sub-assemblages were designed according to the prescriptions of Eurocode 4 and Eurocode 8. As shown, due to the FE modelling assumptions, a rather close agreement was generally found between the FE predictions and the corresponding test measurements, both in terms of global and local phenomena. Therefore, it is first expected that such numerical approach could be implemented as an alternative to costly and time consuming full-scale experimental tests, allowing an extensive parametric investigation of composite joints and possible design optimizations. An implicit advantage of the implemented FE model, in fact, is that according to a refined analysis of the experimental and numerical results for the welded joint object of investigation, the efficiency of the Eurocode 8 design prescriptions for steel-concrete composite joint details can be critically discussed and reviewed. In the specific case, a possible improvement of the design recommendations for the slab reinforcement around the column is proposed.

© 2017 Elsevier Ltd. All rights reserved.

1. Introduction

The behaviour of composite joints is a major issue for steel-concrete composite moment resisting frames subjected to seismic loads; many studies [1–3] investigated their influence on the seismic response of frames considering different design strategies. The current design procedures are based on experimental results and numerical analyses carried out by various researchers mainly in the last 20 years.

The main results of tests on composite joints carried out until 1989 are summarized in [4], then further monotonic and cyclic tests have been carried out on various type of full-scale composite joint sub-assemblages representing exterior and interior beam to column connections [5–16].

The majority of tests past has been performed to study the stiffness, strength, ductility, and energy dissipation capacity of the sub-assemblages and emphasized the effects of deformation of the composite slab and the panel zone (e.g. [6]).

Simões et al. [8–9] focused on the identification of the concrete confinement contribution on composite columns, as well as on the assessment of strength and stiffness degradation. Experimental tests allowed then to study the effect of load path, identifying the corresponding failure modes and fitting the corresponding hysteretic curves by means of the Richard-Abbott and Mazzolani models [16–17].

Green et al. [10] showed that two failure modes must be considered in the design of a composite joint subjected to large cyclic bidirectional loads: a “punch through” of the column web due to force transfer from the “pinned” side of the connection and a crushing mechanism of the concrete slab in contact with the column. More generally, connections with dissipation occurring in the joints components have been tested to verify the influence of the concrete slab and its reinforcement around the column (e.g. [15]), the presence of a cantilever edge strip in exterior joints, the direction of the ribs of the steel sheeting, the presence of supplementary column web panel and stiffeners.

Finite-Element (FE) numerical models related to several experimental tests have been also proposed in the last years, in order to predict the global inelastic response (both monotonic and cyclic) of exterior and interior beam-to-column joints [18–22]. Anyway, the experimental tests on composite joints conducted so far and the

* Corresponding author at: University of Trieste, Department of Engineering and Architecture, Piazzale Europa 1, 34127 Trieste, Italy.

E-mail address: bedon@dicar.units.it (C. Bedon).

corresponding FE numerical representations, although available in a large number in the literature, have been mainly focused on the prediction of the global behaviour only. Differing from existing research projects, this paper focuses on the FE numerical prediction of both global and local behaviour of steel-concrete composite joints.

To this aim, two full-scale exterior steel-concrete composite joints were designed according to the Eurocode 8 and 4 provisions [23,24] and characterized by the presence of two types of connections, i.e. a steel bolted extended endplate connection and a welded connection.

Cyclic experiments were then carried out on both specimens; see [25,26] for a description of the experimental program.

In this paper, as an intermediate stage of an extended research investigation, careful attention is paid to the FE numerical modelling of the welded connection only, which exhibited some relevant mechanisms during the past experiment. The specimen, tested under cyclic loading, was in fact extensively instrumented and a wide range of parameters was monitored during the experimental test. In this respect, the experimental setup and measurements are first recalled from [25].

Based on both global and local available test measurements, the consistency and accuracy of a refined Finite-Element numerical model is then proposed and critically discussed. The main advantage of the presented 3D FE numerical model, implemented in ABAQUS [27,28], is that the actual geometrical and mechanical properties of the joint components, as well as their reciprocal interaction, can be properly taken into account. Given the rather close agreement between experimental results and FE numerical predictions, in particular, it is expected that such numerical approach could be implemented as an alternative to costly and time consuming experimental tests, allowing an extensive parametric investigation of composite joints, including a wide set of geometrical and mechanical configurations for steel-concrete structural systems. An implicit advantage of the same FE modelling approach, as also discussed in this paper, is given in fact the critical discussion and possible review of the design recommendations actually provided by the Eurocode 8 for the steel-concrete composite joints.

2. Past experimental test

2.1. Specimen geometrical details and material properties

Through the FE exploratory investigation, the exterior full-scale composite welded joint (hereinafter called WJ) investigated in [25,26] was taken into account. As shown in Figs. 1–4, the WJ specimen was characterized by the presence of a 330 mm-long (from the external flange of the column) concrete cantilever edge strip and a 2000 mm-long (from the internal face of the column) IPE240 steel beam section directly welded to a 3400 mm-long HE280B partially encased composite column section. Table 1 collects the main features of the steel profiles that were taken into account for the design of the composite beam and column, at the time of the experimental research project.

The steel beam was connected with a 1000 mm-wide and 120 mm-thick concrete slab by means of two 100 mm × 19 mm diameter headed studs placed every 150 mm. The number of shear studs was calculated to ensure a full shear connection between the slab and the beam [24]. The arrangement of the shear studs is shown in Fig. 2(a) and (b). The slab was cast on a trapezoidal steel decking profile and reinforced with six U-shaped longitudinal rebars of 14 mm in diameter (Fig. 2(c)). Furthermore, three transversal rebars of 20 mm in diameter (Fig. 2(c)) were added in front of the column as per Eurocode 8 – Annex C [23].

The concrete region comprised between the column flanges was reinforced with four 12 mm-diameter longitudinal rebars, while 8 mm-diameter rebars welded to the column web were used as stirrups. The stirrups were 40 mm-spaced for a total length of 450 mm from the top and bottom flanges of the beam, and 150 mm-spaced elsewhere (Fig. 3(b)).

The partially encased composite column was pinned at both ends and 10 mm-thick transversal web stiffeners were added at the locations where the vertical load was applied (i.e. 1660 mm from the internal flange of the column) to prevent premature web buckling due to the concentrated load. 10 mm-thick full depth longitudinal stiffeners were also added at the beam-column intersection.

In terms of mechanical properties, the actual concrete compressive strength was characterized by means of standard tests carried out on two 300 mm-height and 150 mm-diameter cylinders. A mean cylindrical compressive strength f_c equal to 24.3 MPa was found (Table 2).

Tensile tests on three specimens were performed to find the actual resistance of the reinforcing bars and of the steel profiles. The average values of the yielding strength, ultimate strength and ultimate strain found for the steel components (rebars, steel flange and steel web) are shown in Table 2. Further details are available in [25].

2.2. Experimental setup, instrumentation and test procedure

As deeply discussed in [25], the cyclic loading history of the past experimental test was based on the ATC-24 protocol [29], see Fig. 5. In accordance with the test setup of Fig. 1, the normal force N was assumed null, while the cyclic vertical forces F (see Fig. 5) were considered as positive when upwards (i.e. sagging bending moment in the beam), and negative when downwards (i.e. hogging moment in the beam).

In order to obtain as much information as possible from each test, a combination of linear transducers and strain gauges was then used to record the displacements and strain in the main specimen components. The arrangement of the LVDTs is shown in Fig. 4(a), while positioning of strain gauges ('sg', in the following) is shown in Fig. 4(b) and (c). A linear potentiometer was also used to measure the deflection at the end of the beam (Fig. 4a). Finally, to better explore the bending behaviour of the concrete slab, three transducers were placed on its top surface.

2.3. Experimental results

2.3.1. Global response

The collapse was reached due to the sudden local buckling of the flange in compression (Fig. 6) which exhibited a wavelength approximately equal to 240 mm, hence coinciding with the height of the steel section. The last cycle of the experiment was also characterized by lateral-torsional buckling due to extensive damage in the concrete slab.

The overall load-displacement cyclic response and the skeleton curves for the welded specimen are shown in Fig. 7. Table 3 summarizes the experimental results characterizing the global behaviour of the joint subjected to sagging and hogging moment, i.e. the displacement and load at yielding (d_y and F_y), the maximum load reached during the loading history and the corresponding displacement (F_{max} and d_{max}) and the ultimate displacement (d_u).

The yielding point was respectively identified with the yielding of the bottom flange of the steel beam under the sagging moment and the yielding of the rebars under the hogging moment [25]. Table 3 also reports the ductility of the connection, calculated as the ratio between the ultimate displacement (d_u) and the yielding displacement (d_y) of the joint. As shown, a ratio greater than 3 for

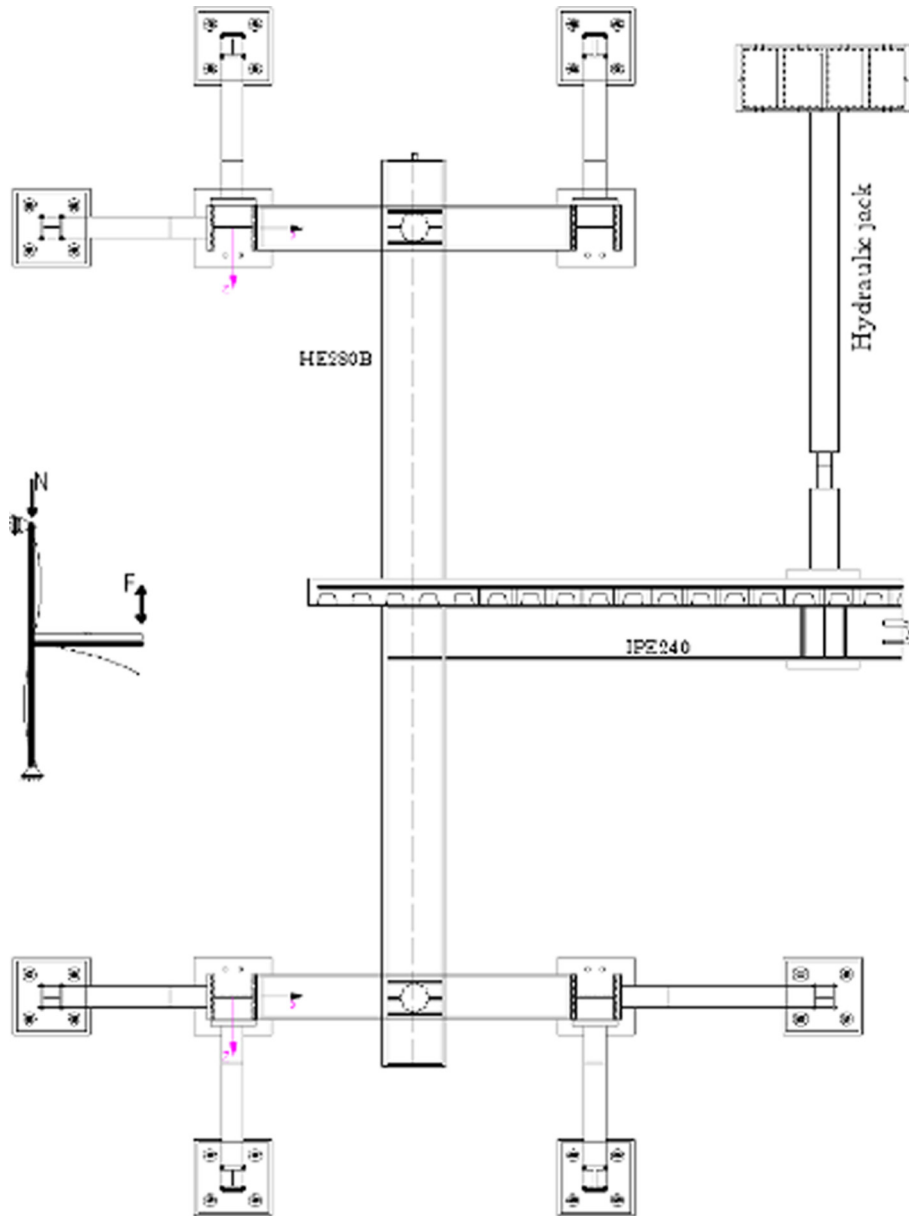


Fig. 1. Test setup, lateral view [25,26].

the specimen under both sagging and hogging bending moments was found. The ultimate inter-storey drift angle d_r is also reported in Table 3. Based on the examined test set-up, the inter-storey drift angle was rationally evaluated in a straightforward way as the ratio between the displacement monitored at the end of the beam and length of the beam itself. A minimum value of 4.4% was obtained under sagging moment, hence resulting in an higher value compared to the provisions of Eurocode 8. Further analysis and critical discussion of the global non-linear behaviour of the specimen (i.e. ductility, dissipation of energy and stiffness degradation) are collected in [25].

2.3.2. Local measurements

In terms of local measurements, the past experimental test highlighted a different participation of the longitudinal rebars with respect to their position along the transverse section, during the loading procedure. This finding is partly emphasized in Fig. 8 (a) and (b) for the S6 and S7 strain gauges, as well as further com-

mented in Section 3, together with the corresponding numerical predictions.

The experimentally observed behaviour is consistent with the shear lag effect and the concept of effective width. For a given loading step and based on the notation of Fig. 4(c), the strain registered by strain gauge S6 resulted in fact clearly smaller than the value monitored in S7. The same comment can be extended also to gauge S17, compared to S19 measurements. Finally, it is worth noting the difference in the slope of the load-rebar strain relationships for the same gauges, as far as the sign of the load changes. This effect can be justified by the absence of the concrete component when the load becomes negative and the beam is subjected to a hogging moment (i.e. concrete slab in tension).

Regarding the evolution of strains in the seismic rebars (see also the comparative curves collected in Section 3), it is interesting to notice that the experimental test showed a rather close correlation with design standards. For the strain gauge S14, for example, the strain was observed to increase for sagging moment when the RC

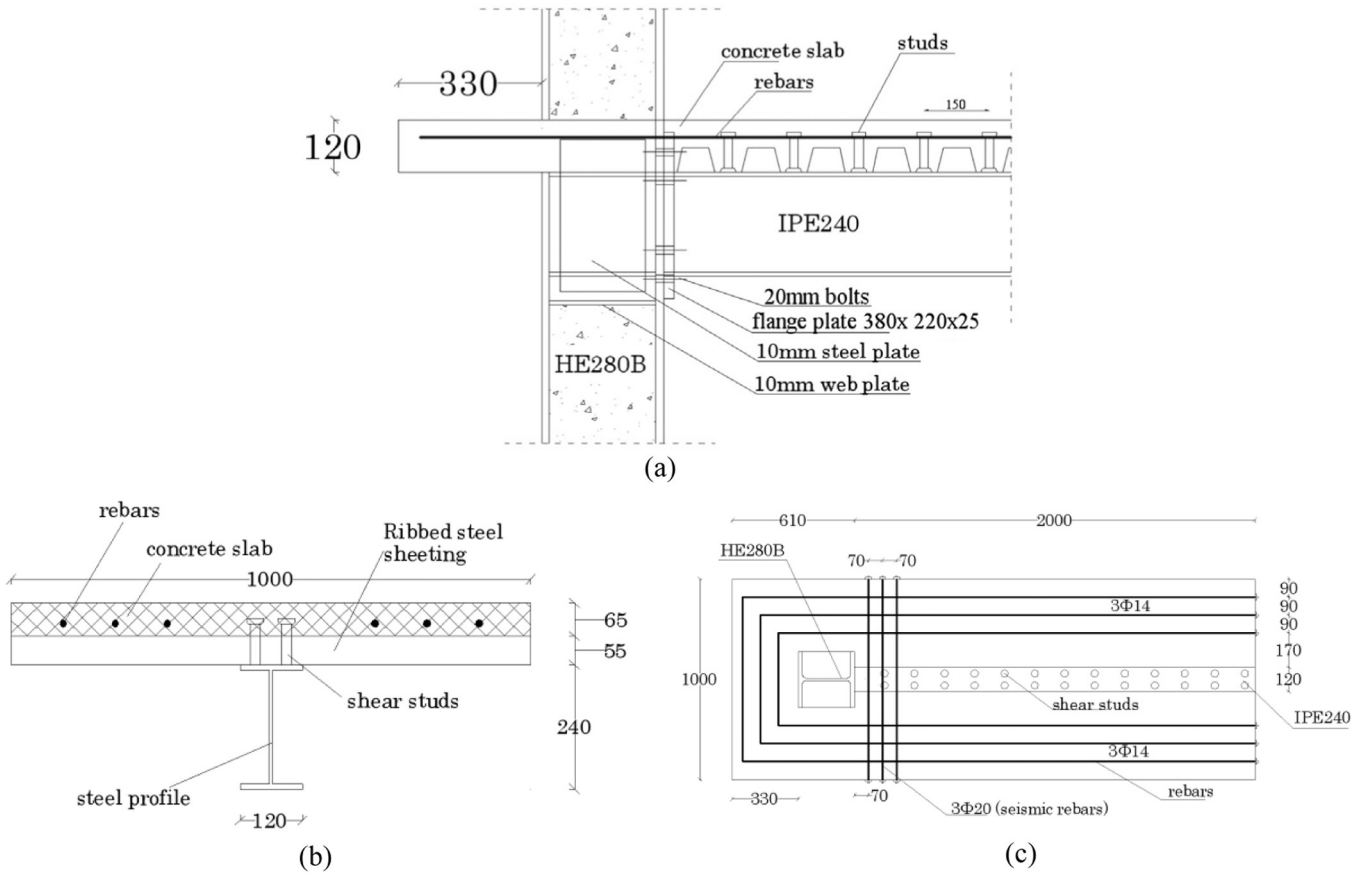


Fig. 2. Geometrical properties of the specimen. (a) Lateral view; (b) cross-section of the composite beam and (c) rebar in the slab, top view [25,26]. Nominal dimensions in mm.

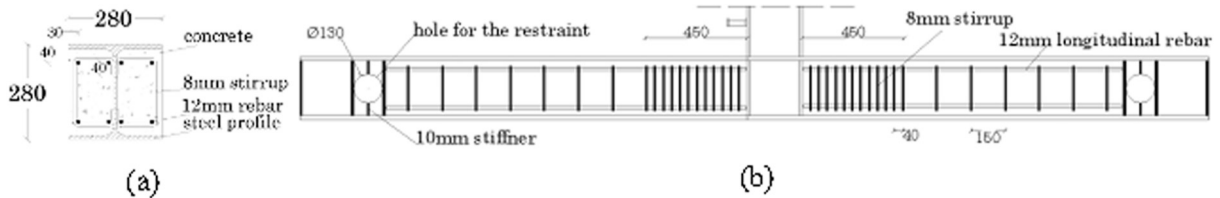


Fig. 3. Geometrical properties of the tested specimens. (a) Cross-section of the composite column and (b) lateral view of the reinforcing bars in the column (90° rotated). Nominal dimensions in mm.

slab is subjected to compression, due to the formation of compression struts (i.e., what is described as mechanism 1 and 2 in Eurocode 8). The same behaviour was also observed in the cantilever concrete edge strip, as far as the assigned load induces a hogging moment on the composite beam. In this latter case, the rebar involved in the mechanisms consisted in U-shaped longitudinal bars (3Φ14, Fig. 2).

Together with strain measurements in the rebar, the overall moment-curvature response of the joint was also monitored, see Fig. 8(c). In the figure, the cyclic response of the specimen is shown, as obtained by the strain gauges on the rebar and the steel joist at a cross-section 65 mm distant from the edge of the column.

The LVDT10 instrument was finally placed on the concrete slab (Fig. 4(a)) to calculate the average strain of the concrete region in contact with the flange of the column (mechanism 1, as for Eurocode 8). Despite the cyclic loading condition (see also section 3), the specimen achieved a strain in compression in the order of ≈0.5%, i.e. markedly higher than the ultimate strain provided by the Eurocode 8.

2.4. Finite-Element numerical modelling

Based on the available experimental test results, a three-dimensional Finite Element model was implemented in the ABAQUS computer software [27,28], to simulate the response of the full scale WJ joint as well as to further explore at the component level the typical structural performance. At the current stage of the research project, only a monotonic, static simulation was carried out.

The intention – once assessed the accuracy and possible critical aspects of the presented FE modelling approach – is to further extend the same methodology to a multitude of geometrical and mechanical configurations of practical interest, including also possible variations in boundary and loading conditions (i.e. cyclic loads).

2.5. Element type, mesh pattern and model assembly

To ensure the accuracy and the computational efficiency of the FE simulations, careful consideration was first paid to the

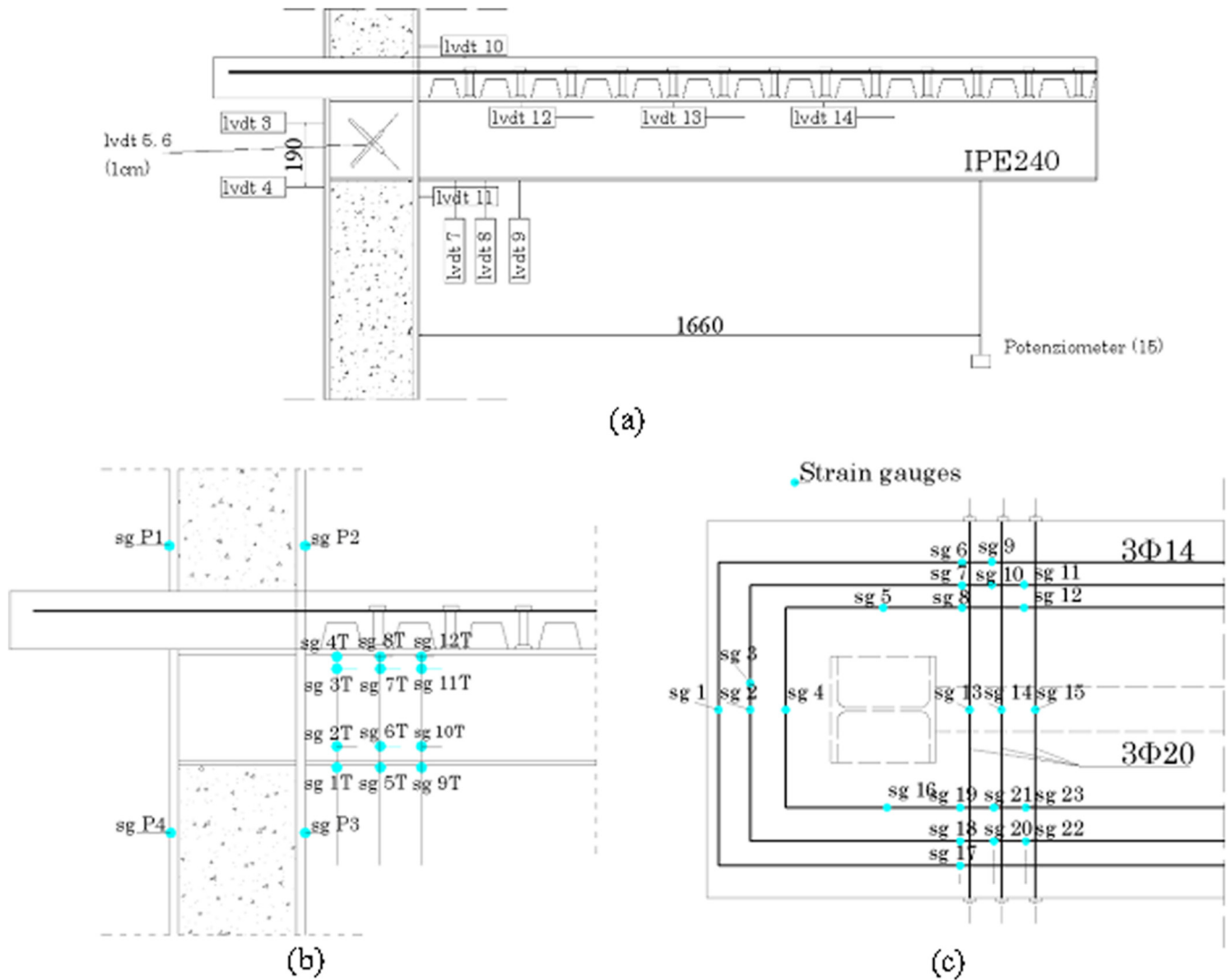


Fig. 4. Instrumentation arrangement for the experimental test: (a) LVDTs, dimensions in mm (lateral view); (b) strain gauges on the steel beam and column (lateral view); (c) strain gauges on the reinforcing bars (top view).

Table 1
Nominal dimensions of the steel profiles.

	ID	B [mm]	H [mm]	t_r [mm]	t_w [mm]
	IPE240	120	240	9.8	6.2
	HE280B	280	280	18	10.5

Table 2
Experimental mechanical properties of the materials (average values expressed in [MPa]).

	24.3		
	f_y	f_t	ϵ_u
Concrete	460	549	15.3
Rebars	309	419	17.3
Steel (flanges)	394	481	13.6
Steel (web)			

geometrical and mechanical characterization of the joint components, as well as to their reciprocal interaction.

Based on the available technical drawings of the full-scale specimen, in particular, the actual geometry of the steel profiles, as well

as the reinforcing bars and the RC components were properly reproduced. A free mesh pattern mainly composed of C3D4 tetrahedral elements was used, with average elements size generally comprised between 4 mm and 60 mm (see Fig. 9). The reinforcing bars were modeled using beam elements (B31 type) fully embedded in the RC components. The shear stud connectors were also embedded in the concrete mesh, while for the sheet decking a distributed, rigid constraint was assigned at the interface with the RC slab and with the base section of the studs. To this aim, the steel decking was described in the form of linear tetrahedral elements (C3D4 type, as in the case of the RC slab), with 1.5 mm the nominal thickness. Circular holes with 19 mm the diameter were positioned in the steel decking in accordance with the technical drawings of the full-scale experimental specimen.

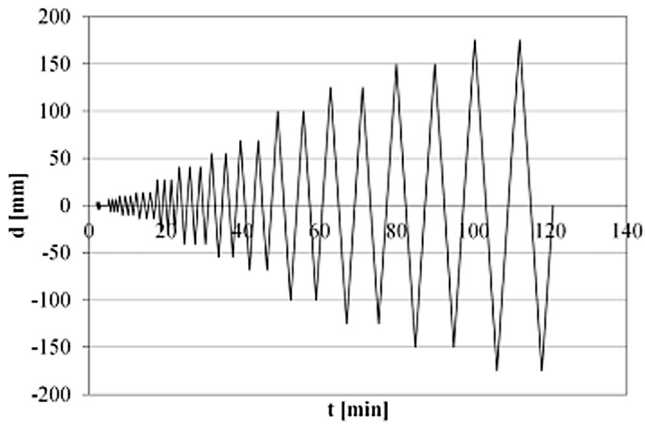


Fig. 5. Loading protocol for the full-scale cyclic experiments.

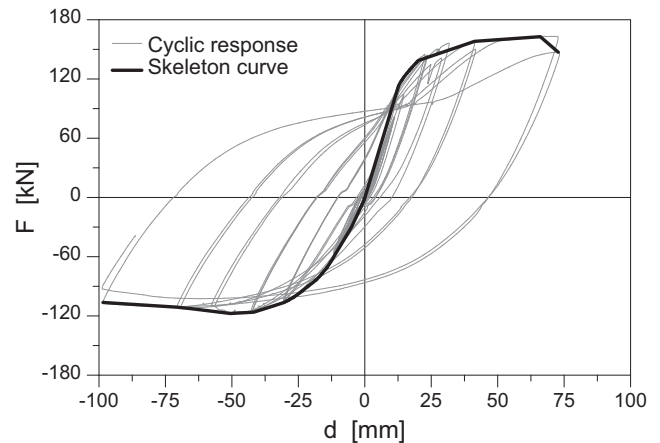


Fig. 7. Experimental cyclic response and skeleton curve for the WJ specimen.



Fig. 6. Failure configuration for the full-scale specimen due to local buckling.

All the welded elements were modeled using the *tie* constraint option available in the ABAQUS library, hence possible relative displacements and rotations, as well as damage phenomena in the vicinity of the connection, were fully neglected.

3. Material mechanical proprieties

3.1. Steel

The structural steel components, such as the beam, the column and the studs, were mechanically characterized by means of an elasto-plastic material model.

The yield and ultimate tensile strengths obtained from the experimental tests carried out on coupons, as well as the corresponding strain values, were taken into account for the implementation of the corresponding constitutive law. Concerning the

Young's modulus and Poisson's ratio, the nominal values of 210 GPa and 0.3 respectively were considered.

A key role in such FE model was given by the overall constitutive law implemented for the steel members. The correct FE prediction of the failure mechanism for the welded composite joint object of investigation – including global as well as local effects – represented in fact the major challenge of this research contribution.

In particular, as observed from post-processing of FE results, numerical singularities proved to represent the reason of important numerical issues in the analyses (although restricted to a limited region of the full 3D model). This is the case of the section of connection between the steel beam and the steel column, where – despite a careful mesh and element type sensitivity study – the traditional Von Mises constitutive law typically resulted in the prediction of inconsistent maximum stresses in the beam.

To overcome such limitations, as well as to ensure the consistency of the estimated FE results, the maximum stresses in steel deriving from the triaxial hydrostatic state were limited by means of the Gurson porous model [30–34], which was implemented in place of the Von Mises constitutive law. The Gurson model is traditionally used in FE numerical practice to overcome the widely used constitutive laws for engineering materials that assume plastic incompressibility, and no effect on yield of the hydrostatic component of stress (as in the case of the Von Mises model). However, void nucleation and growth (and thus bulk dilatancy) are commonly observed in some processes which are characterized by large local plastic flow, such as ductile fracture. The aim of this model is hence to develop approximate yield criteria and flow rules for porous (dilatant) ductile materials, showing the role of hydrostatic stress in plastic yield and void growth.

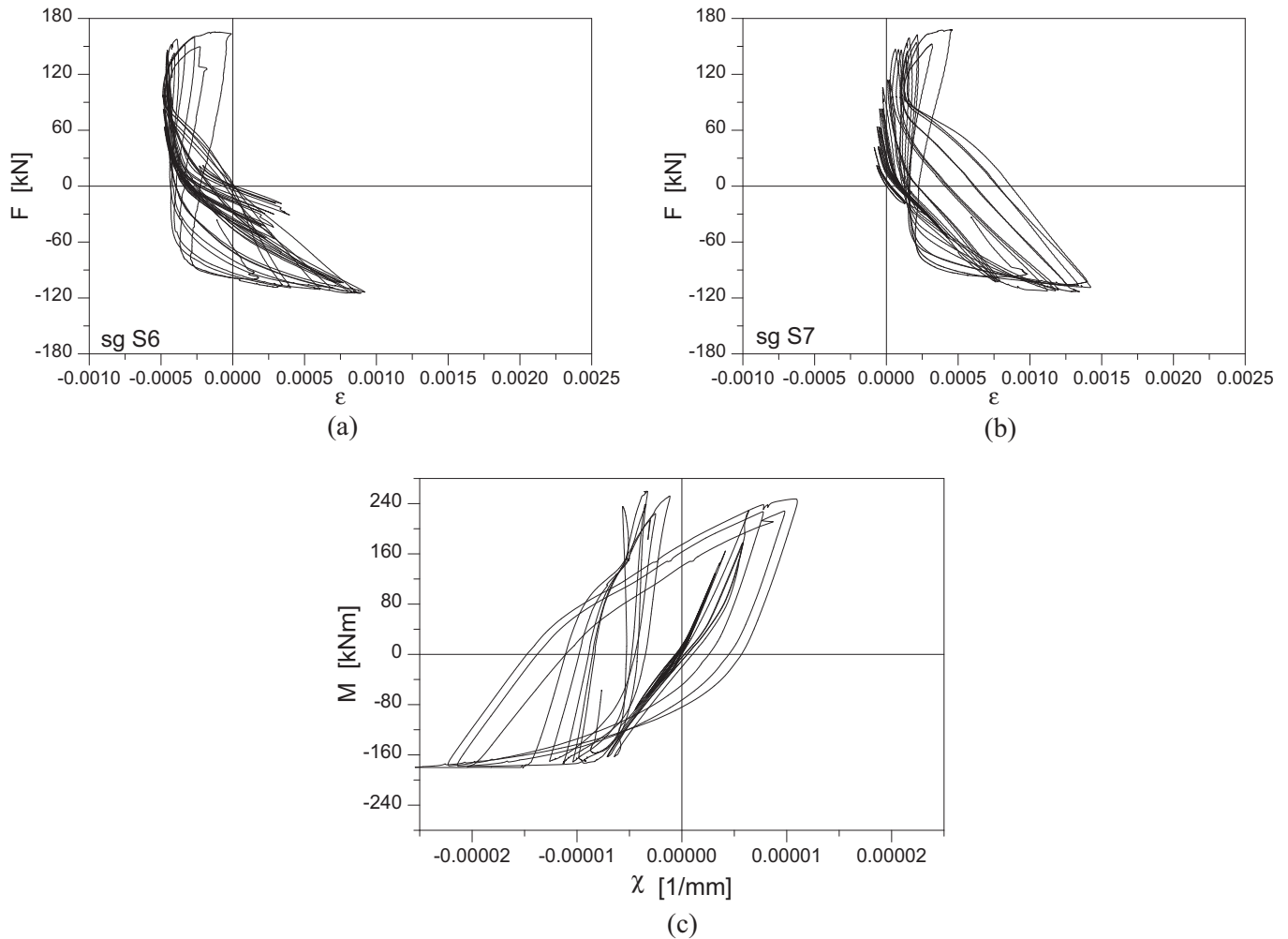
For FE simulations aimed to describe fracture mechanisms of ductile metals, the Gurson-Tvergaard material model available in ABAQUS can be used to explain local strength decrease during damage propagation, in the intermediate phase between the nucleation and coalescence of voids. In it, nucleation and coalescence are in fact taken into account before homogenization by applying appropriate corrections directly to the stress-strain cell response. The homogenization technique is based on the stress-strain characterization of a representative volume element that is considered to be a cubic volume with voids before the material is stressed. In such formulation, a key role is assigned to the coefficients q_1 , q_2 , and q_3 representative of the critical yielding surface definition (Eq. (1)), see also [27,28]:

$$\phi = \left(\frac{q}{\sigma_y}\right) + 2q_1 f \cosh\left(-\frac{3}{2} \frac{q_2 p}{\sigma_y}\right) - (1 + q_3 f^2) = 0 \quad (1)$$

Table 3

Global experimental results for the WJ specimen under sagging and hogging moment.

	d_y [mm]	d_{max} [mm]	d_u [mm]	d_u/d_y [-]	d_r [%]	F_y [kN]	F_{max} [kN]
Sagging moment	12	66	73	6.08	4.40	115	165
Hogging moment	-28	-50	-98	3.50	5.90	-101	-115

**Fig. 8.** Experimental measurements for the WJ specimen. (a)–(b) Stress-strain relationship in the sg S6 and sg S7 rebars and (c) moment-curvature relationship measured at a distance of 65 mm from the column edge.

In Eq. (1), in particular, q is the Von Mises stress, p is the hydrostatic pressure, σ_y is the yield stress, q_1 , q_2 , and q_3 are the Tvergaard correction coefficients, while f ($0 \leq f \leq 1$) is the void volume fraction, which is defined as the ratio of the volume of voids to the total volume of the material and is defined as:

$$f = 1 - r. \quad (2)$$

In Eq. (2), r is the relative density of the material (with $f = 0$ for a fully dense material, hence the Gurson yield condition reduces to the Mises model, and $f = 1$ for a material without any stress carrying capacity). In accordance with [34], the input parameters for the current study were set equal to $r = 0.96$, $q_1 = 1.5$, $q_2 = 1$ and $q_3 = q_1^2 = 2.25$.

3.2. Concrete

The concrete damaged plasticity (CDP) model was used through the numerical investigation, see Fig. 10. The main advantage of the

CDP model is that such modelling assumption provides the ability to analyze concrete structures under static or dynamic cyclic or monotonic loading based on a damaged plasticity algorithm. In order to ensure the accuracy of FE results, the mechanical calibration of the CDP input parameters – both for the tensile and compressive constitutive behaviour – was carried out in accordance with [35,36], as well as on the base of the experimental results derived from the small concrete specimens (see Section 1 and [26]).

Assuming a nominal ultimate strain for concrete $\varepsilon_c = 0.0035$ (Ref. [36]), in particular, the compressive stress-strain constitutive law for the CDP formulation takes the form:

$$\frac{\sigma_c}{f_{cm}} = \frac{k\eta - \eta^2}{1 + (k-2) \times \eta} \quad (3)$$

where the compressive stress σ_c in concrete at a given strain level ε_c depends on the ratio:

$$\eta = \frac{\varepsilon_c}{\varepsilon_{c1}} \quad (4)$$

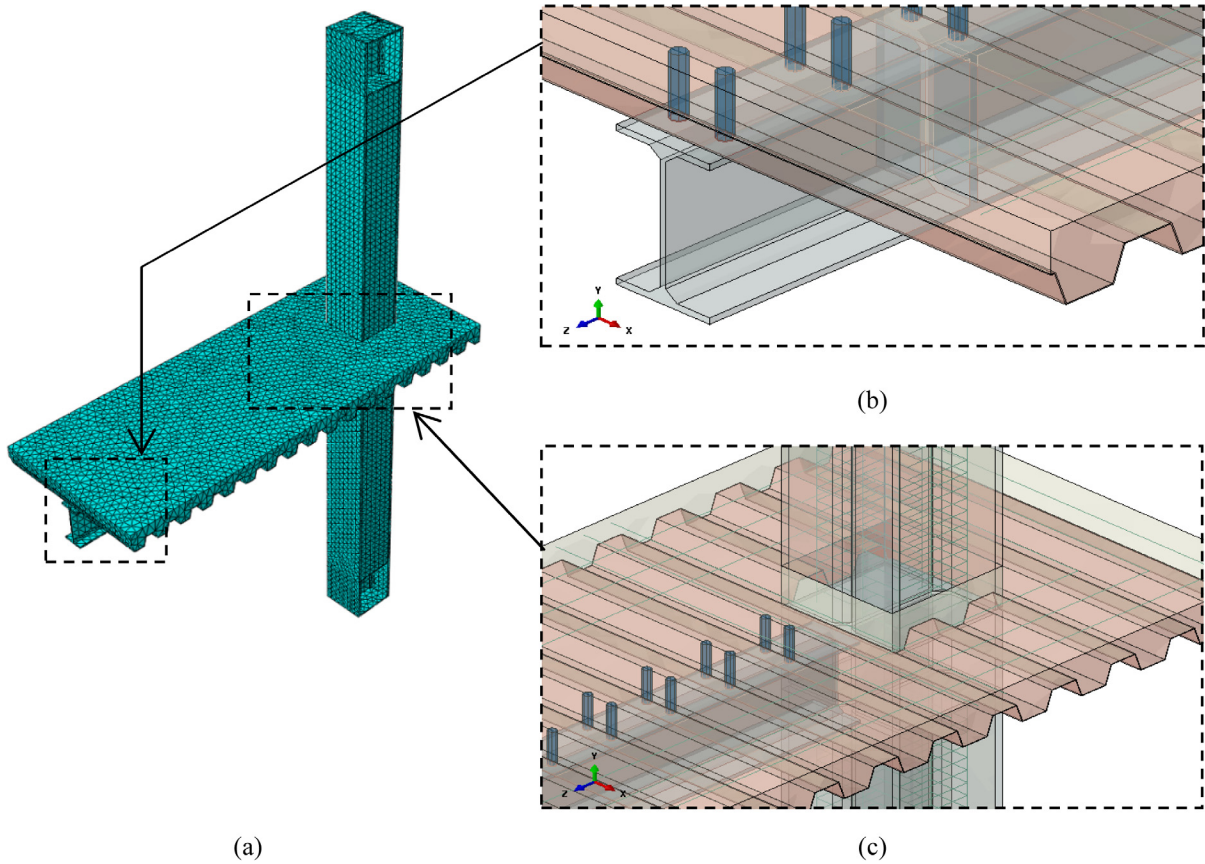


Fig. 9. 3D Finite Element model of the WJ specimen (ABAQUS): (a) model assembly (axonometry) and (b)-(c) geometrical details.

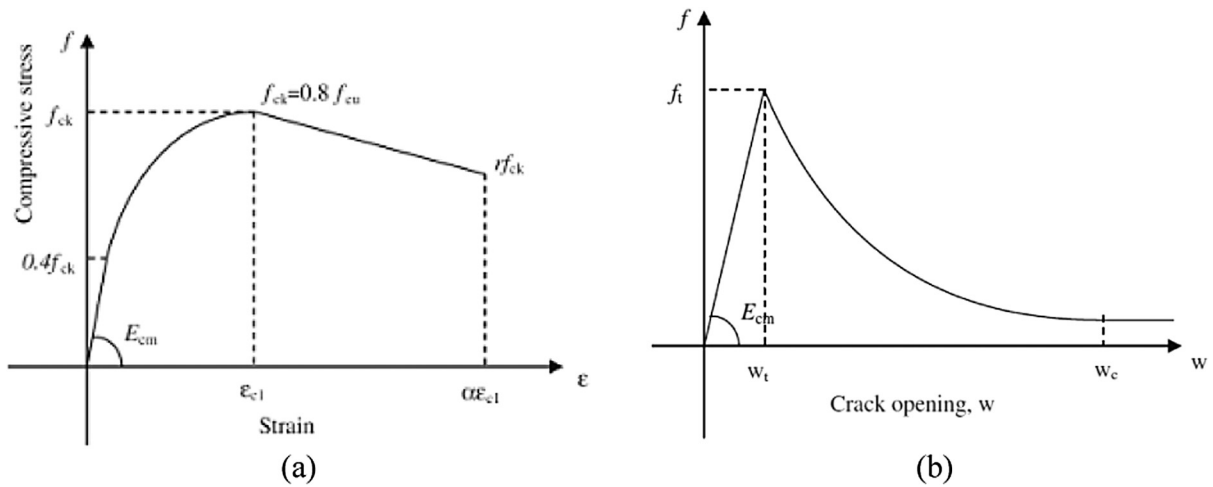


Fig. 10. Constitutive laws implemented in ABAQUS for concrete (a) in compression and (b) tension.

with

$$\epsilon_{c1} = 0.7f_{cm}^{0.31} \leq 2.8, \tag{5}$$

being Eq. (5) representative of the compressive strain in concrete at the peak compressive stress, and

$$k = \frac{01.05E_{cm} \times \epsilon_{c1}}{f_{cm}}. \tag{6}$$

The non-dimensional stiffness degradation parameter d_c (i.e. equal to 1 for fully cracked concrete and equal to 0 for uncracked concrete, respectively), representative of crushing damage of concrete was then also defined as [27,36]:

$$d_c = 1 - \frac{\sigma_c/E_{c0}}{\epsilon_c^{pl} + \sigma_c/E_{c0}} \tag{7}$$

with $E_{c0} = E_{cm}$ the initial elastic modulus derived from the experimental tests and ϵ_c^{pl} the equivalent plastic strain, being defined as a function of the inelastic strain ϵ_c^{in} :

$$\epsilon_c^{pl} = b_c \times \epsilon_c^{in} = b_c \times (\epsilon_c - \sigma_c/E_{c0}), \tag{8}$$

while $0 \leq b_c = 0.7 \leq 1$ is a compressive coefficient calibrated in accordance with [37].

In terms of tensile behaviour of concrete, a similar approach was followed. The stress-strain constitutive law, in this case, was defined as [27,36,38,39]:

$$\frac{\sigma_t}{f_t} = f(w) - \frac{w}{w_c} f(w_c) \quad (9)$$

with

$$f(w_c) = \left[1 + \left(\frac{c_1 w}{w_c} \right)^3 \right] \exp \left(-\frac{c_2 w}{w_c} \right) \quad (10)$$

where w represents the crack opening displacement, while

$$w_c = 5.14 \frac{G_f}{f_{ct}} \quad (11)$$

is the crack opening displacement at which stress can no longer be transferred.

In Eq. (9), moreover, $c_1 = 3$ and $c_2 = 6.93$ are two material constants (values in use for Normal Weight Concrete), while f_{ct} in Eq. (11) can be calculated as [27]:

$$f_{ct} = 0.7 \times (0.3 f_{ck}^{2/3}) = 0.7 \times (0.3 \times (f_{cm} - 8)^{2/3}). \quad (12)$$

In Eq. (11), finally, the fracture energy of concrete was estimated as (see [40]):

$$G_f \approx \frac{G_F}{2.5} \quad (13)$$

A reference value of 0.15 N/mm was assumed for the base value of fracture energy G_F , based on the average size of aggregates for the examined experimental specimen.

3.3. Boundary conditions, loading procedure and solving method

The assembled FE model was properly restrained, in order to reproduce the ideal restraint conditions of the tested full-scale specimen (see Fig. 1). The monotonic response under both sagging and hogging moment was then separately explored. The typical simulation, as a result, consisted in a linear geometrical, static step in which monotonic loads were linearly increased up to failure.

4. Discussion of results

4.1. Global response

The monotonic, global response of the WJ joint was first investigated. In general, despite the geometrical and mechanical assumptions of the implemented FE model, a rather close agreement was found between FE results and corresponding experimental predictions. Fig. 11 presents an experimental and numerical load-displacement comparison for the examined WJ joint. In the figure, two plots are provided for the reference FE model, i.e. by assuming a Von Mises constitutive law only for the steel members ('VM' curve), as well as by using the Gurson model ('G' curve).

As also observed during the post-processing analysis of the so obtained FE results, the implementation of the Gurson model proved to have important local effects at the component level (i.e. evolution of stresses at the connection between the beam and the column), compared to the Von Mises constitutive law. These effects were visible from the first loading phases, following the first yielding of the steel components. At the same time, no important variations were observed in the corresponding overall load-displacement curves for the examined joint (see Fig. 11).

In terms of calibration of the input Gurson parameters, moreover, it is interesting to point out that a further sensitivity study (not included in the paper, for space limitations) highlighted a rather negligible sensitivity of the overall FE predictions to the

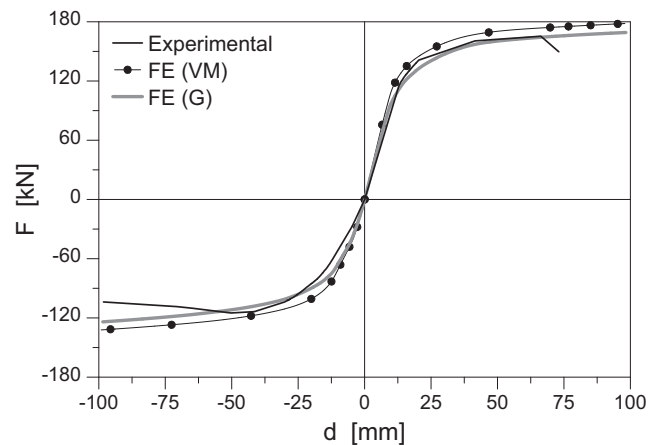


Fig. 11. Experimental and FE load-displacement curves. (VM = Von Mises; G = Gurson).

Gurson input parameters themselves (i.e., as far as q_1 , q_2 and q_3 are assumed within their range of validity). As a result, the FE model including the Gurson mechanical law ('G') was kept as reference model for all the comparative calculations proposed in Section 4.2.

In general terms, see Fig. 11, major discrepancies between the collected numerical and experimental data can be found especially in terms of initial stiffness – being lightly overestimated by the FE model – as this parameter is strictly related to the implementation and mechanical calibration of surface-to-surface interactions and contacts between the specimen components.

The same discrepancies could also be justified by the monotonic – rather than cyclic – load introduction through the FE study, hence fully disregarding the cyclic degradation of the materials mechanical properties, as occurred during the experiment. In this regard, the major limit of the implemented FE model proved to be represented by the lack of marked softening phenomena, compared to the experimental test results. Rather good global predictions were found, in any case.

Under hogging moment, as shown in Fig. 11, the FE model overestimates the experimental initial stiffness in the order of $\approx 14.2\%$. The specimen failed at a maximum load F equal to ≈ 110 kN. The collapse of the specimen derived from yielding of the beam flange in compression, as also highlighted by an important peak of maximum compressive stresses in the beam web and flanges (Fig. 12). In this regard, it is also interesting to notice that local buckling of the beam flange in compression was properly captured by the FE model. Close correlation between FE and experimental results was found also under sagging moment, see Fig. 11. As in the case of hogging moment, local buckling in the steel beam was again noticed.

In terms of stress distribution in the concrete slab, both stress scenarios numerically observed for the WJ model under sagging and hogging moment highlighted a rather close agreement with the collapse mechanisms provisions described by the reference design standard [24], see Fig. 13. In the figure, for clarity of presentation, the concrete infill comprised within the column flanges is hidden. As shown, the compression stresses in the concrete (negative values) are mainly located in the contact zone between the slab (the cantilever part in case of hogging moment) and the column (flange and web). The FE simulations also exhibited a tensile damage propagation in the concrete slab, starting from vertical deflections in the order of ≈ 8 – 10 mm. Also in this case, rather close agreement was found with the corresponding experimental crack pattern (see Fig. 14).

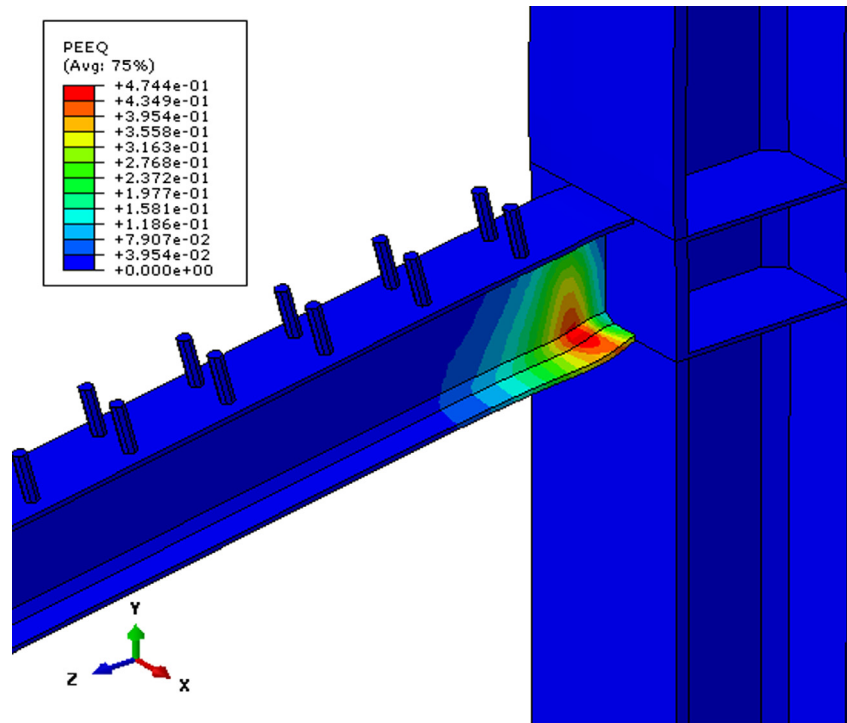


Fig. 12. Plastic hinges in the structural steel components of the WJ model at collapse, under hogging moment.

4.2. Local response

Local comparisons were then carried out on the same WJ model.

First, the experimentally measured strains in the rebar were compared with the corresponding FE predictions, as a function of the applied load F , by taking into account few key control points, see Fig. 15. As in the case of the experiment, a different distribution of maximum deformations was observed in the FE rebars, depending on their position within the RC slab.

In general, a good correlation was noticed by comparing the FE results and the experimentally measured local strains (see Fig. 16), hence suggesting the accuracy of the implemented FE model.

The FE model exhibits the occurrence of a first negative deformation of the longitudinal rebar and the ultimate deformation of S19, which is closer to the column than S17. The difference between the numerical and experimental responses is significant in the intermediate phase. This effect, as also previously pointed out, could be probably justified by the different load histories (FE being monotonic rather than following the experimental cyclic protocol).

Fig. 16(c) and (d) further compare the force–deformation responses of the seismic rebar. In this latter case, the FE model correctly predicts the response as experimentally measured at the S2 location, where the largest deformation under hogging moment was attained. A similar qualitative response was found at the S14 location (see Fig. 16(d)), for the seismic rebar close to the interior part of the column, where maximum deformations under sagging moment occurred.

To compare the concrete mechanism response, a final attempt was carried out by exploring the stress distribution in the slab. Fig. 17(a), to this aim, shows the location of the FE control point that was taken into account for comparison with the WJ specimen measurements (with 135 mm the distance from the column flange, i.e. in agreement with the position of the LVDT10 instrument).

From Fig. 17(b) it is possible to notice that the load–strain relationship in the region of concrete in contact with the column was

appropriately simulated for the WJ specimen under sagging moment (i.e. RC slab in compression). Under hogging moment, poor correlation was found between FE and experimental data.

The FE response of the joint was in fact characterized by limited deformations in concrete, due to the full detachment of the slab from the column flange. As a direct effect of the loading protocol, the FE overestimation of the experimental load–strain relationship can be further justified by the presence – in the WJ cyclic experiment – of a larger gap at the interface between the RC slab and the column flange, while this effect was fully neglected in the corresponding numerical simulation.

In order to compare the moment–curvature relationship of the composite beam, two monitored points (strain gauges S20 on the longitudinal rebar and T5 on the steel beam) located at a distance of 143 mm from the column flange were finally taken into account, see Fig. 18(a). As shown in Fig. 18 (b), FE results in rather close agreement with the corresponding experimental relationships were obtained, both in terms of stiffness and resistance, hence giving further evidence of the FE model accuracy.

4.3. Analysis of the joint steel components contributions

A final validation and comparison between the FE predictions and the corresponding experimental test was then carried out by taking into account the separate contribution of the joint components (i.e. the steel beam, the steel column, the column web panel) on the global structural performance of the WJ specimen.

In accordance with the experimentally derived steel component contributions of the WJ specimen (see Fig. 19(a) and [25]), where the beam proved to have a predominant role on the structural performance of the WJ specimen, the FE model further highlighted a major plastic damage propagation in the steel beam, with a fully elastic performance of the column and an almost negligible plastic deformation in the column web panel.

In Fig. 19(b) to (d), a qualitative evolution of plastic hinges is proposed for the FE model under sagging moment, at few selected

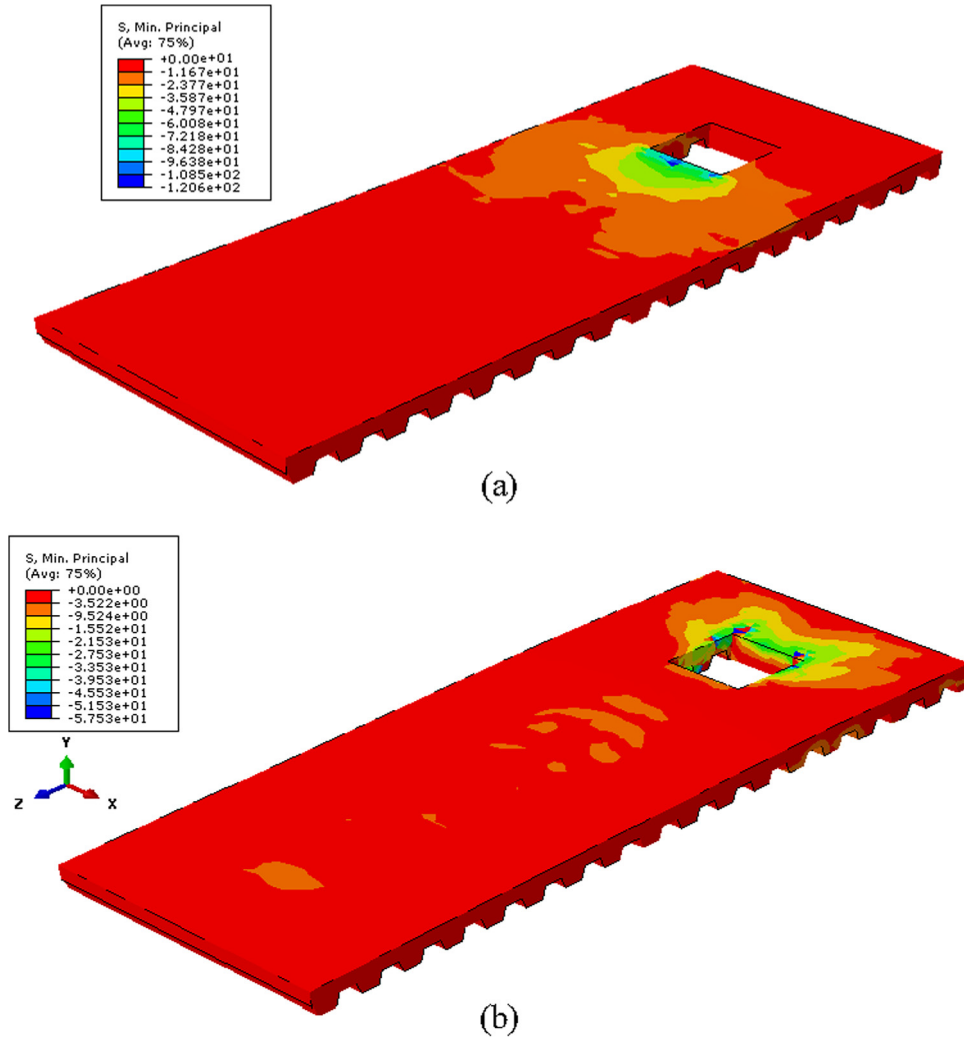


Fig. 13. Distribution of compressive stresses in the concrete slab under (a) sagging and (b) hogging moment, as observed at a vertical deflection $d = 40$ mm (scale factor = 1). Values of stresses expressed in MPa.

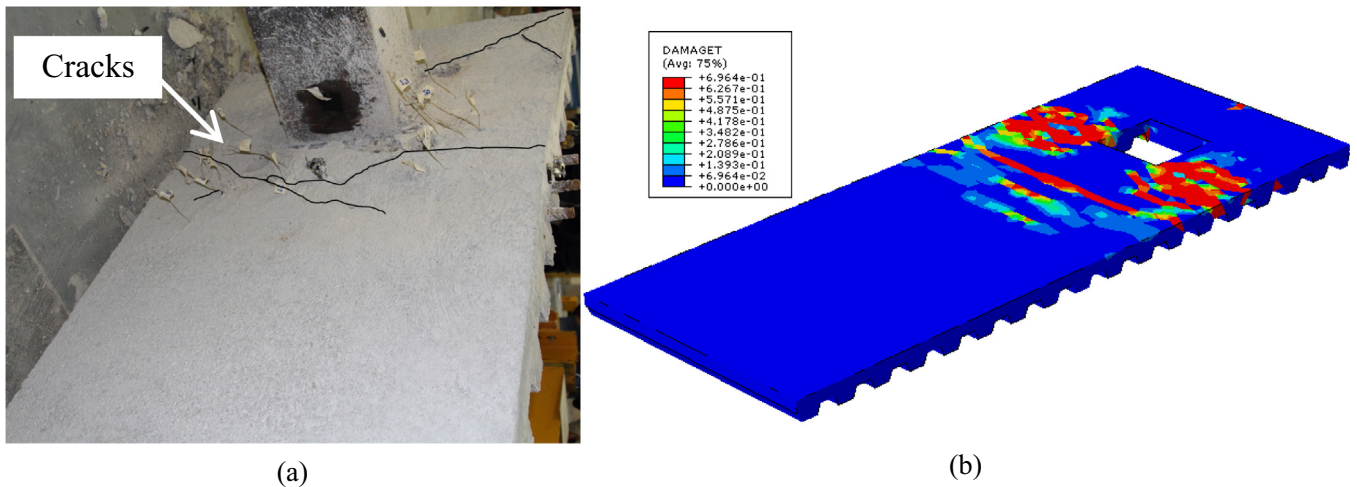


Fig. 14. Distribution of cracks in the concrete slab, as observed (a) experimentally and (b) numerically (example provided for the FE model under hogging moment, at a vertical deflection $d = 10$ mm, scale factor = 1).

displacement amplitudes (20 mm, 30 mm and 40 mm respectively). An accurate analysis of experimental and FE results highlighted that the first plastic deformations occur in the beam, as

far as the applied sagging moments attains the value of ≈ 200 kNm, hence corresponding to a vertical load $F \approx 120$ kN and a beam deflection of ≈ 10 mm. As far as the beam deflection

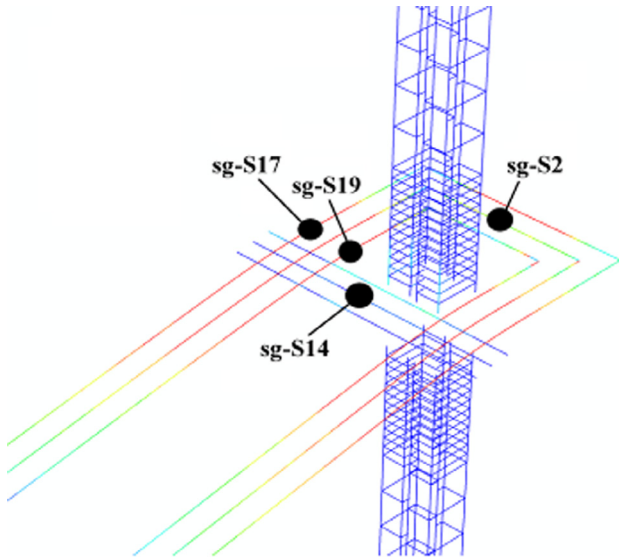


Fig. 15. FE control points for the measurement of maximum stresses in the longitudinal and seismic rebars.

increases, see Fig. 19(b) to (d), the plastic deformations further magnify in the beam itself. Through the full FE simulation, compared to the beam, the column web panel exhibited negligible plastic deformations only, i.e. $\approx 8\text{--}10$ times lower than the beam

itself. This finding is emphasized in Fig. 19(b) to (d), and manifests a rather close agreement with the experimental data provided in Fig. 19(a).

5. Discussion on the design of the seismic rebar

A final critical analysis of the experimental and numerical results shows that the overall behaviour of the joint under sagging moment has been influenced by the resistance of the seismic transversal rebars arranged in front of the column and designed according to Eurocode 8 - Annex C [23]. The purpose of these rebars is to ensure the formation of compression struts in contact with the faces of the column, allowing to transfer the composite action recovered by the slab to the column.

The presence of struts is dependent on the nodal configuration. Adopting the Eurocode 8 Annex C nomenclature, mechanism 1 – direct compression on the column flange – and mechanism 2 – compressed concrete struts inclined to the column sides – may form for the tested specimen.

The maximum compressive force transmitted to the column through each mechanism is [23]:

$$F_{Rd,1} = b_b d_{eff} (0,85 f_{ck} / \gamma_c) \tag{14}$$

$$F_{Rd,2} = 0,7 h_c d_{eff} (0,85 f_{ck} / \gamma_c) \tag{15}$$

where b_b is the bearing width of the concrete of the slab on the column, d_{eff} is the overall depth of the slab in case of solid slabs or the

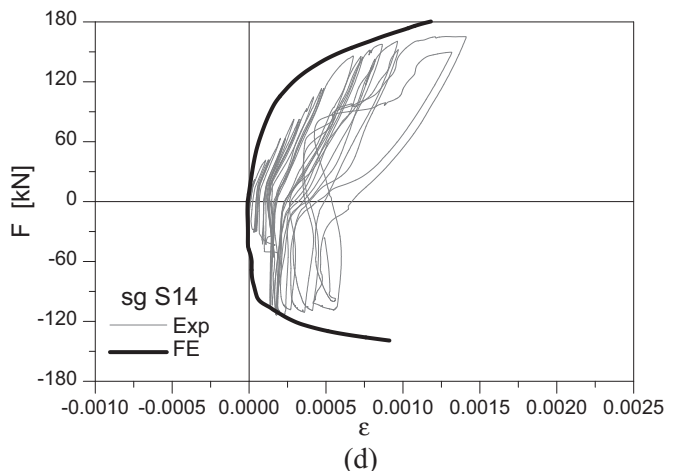
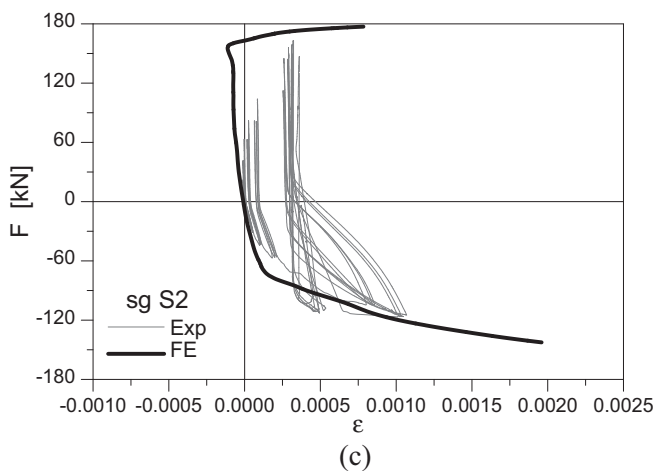
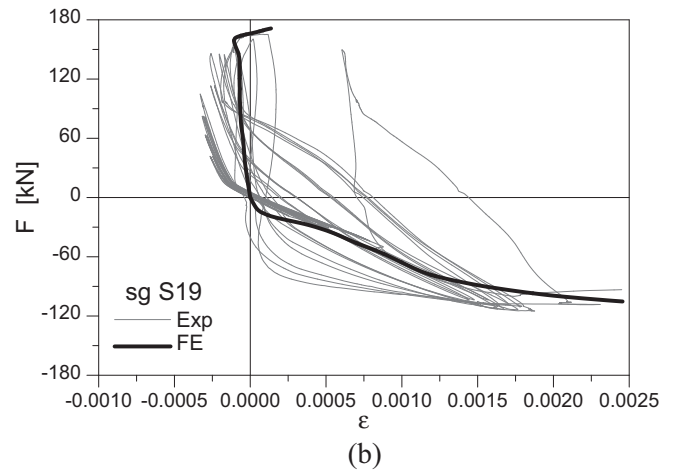
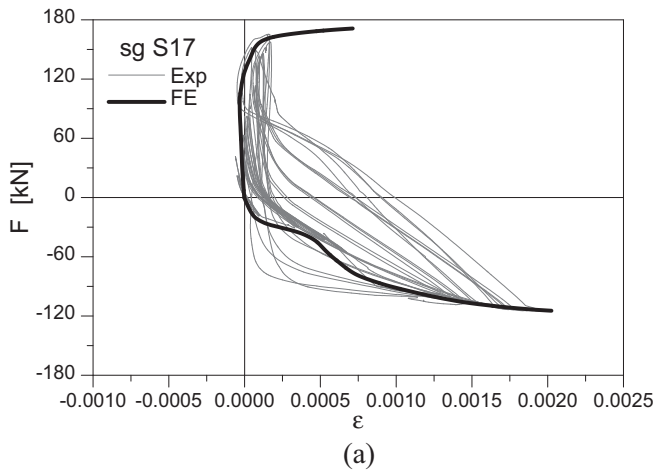


Fig. 16. Load-strain relationships for the longitudinal and seismic rebars: comparison between FE estimations and experimental measurements (cyclic curve), as obtained from strain gauges (a) S17, (b) S19, (c) S2 and (d) S14.

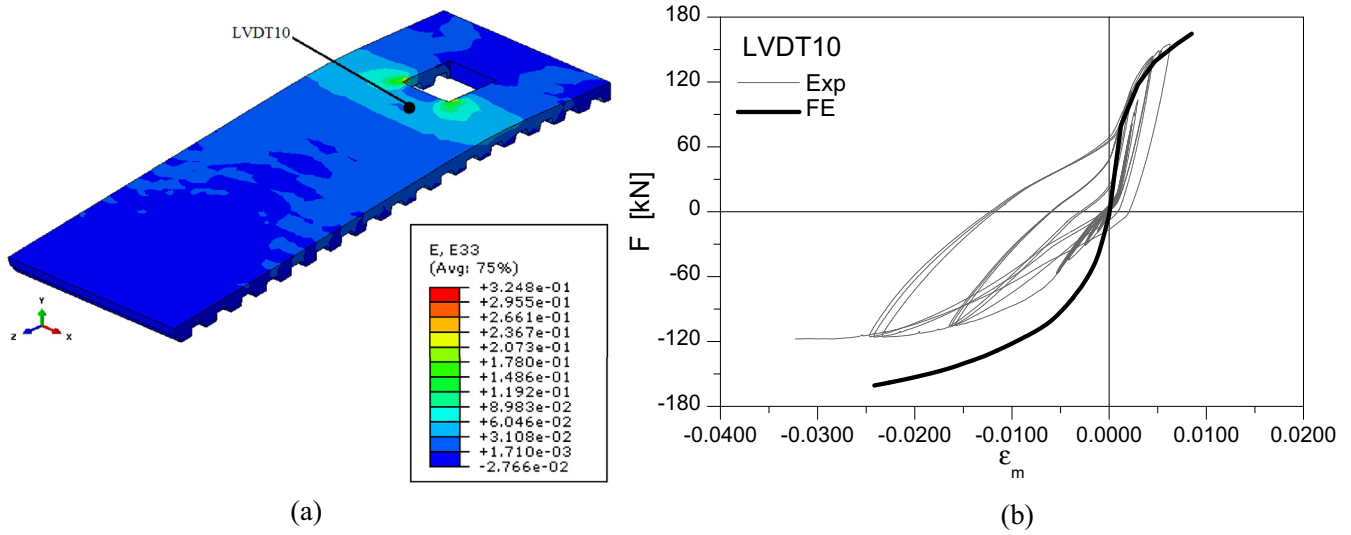


Fig. 17. (a) FE control point corresponding to the LVDT10 instrument (contour plot of strains), and (b) load-strain comparisons for the response of the concrete slab in the vicinity of the column.

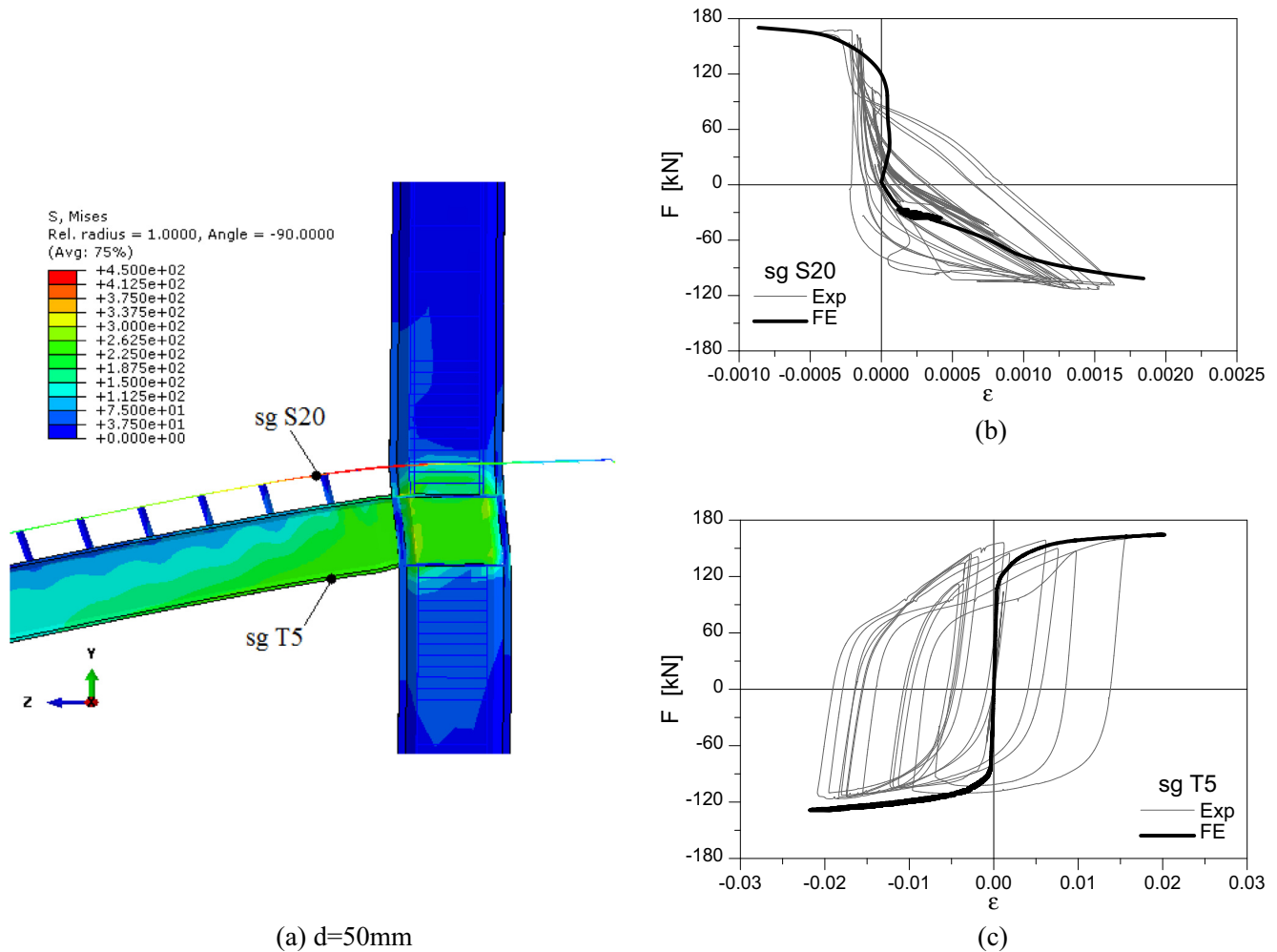


Fig. 18. (a) FE control points associated to the S20 and T5 instruments, with contour plot of stresses expressed in MPa ($d = 50$ mm), and corresponding (b)-(c) load-strain comparisons.

thickness of the slab above the ribs of the profiled sheeting for composite slabs, h_c the height of the column, f_{ck} the characteristic concrete compressive strength and γ_c the concrete partial safety factor.

In the Eurocode approach, the seismic transverse reinforcement must be such as to allow the complete crushing of the struts, so the maximum value of the compressive force transmitted by the slab can be taken as:

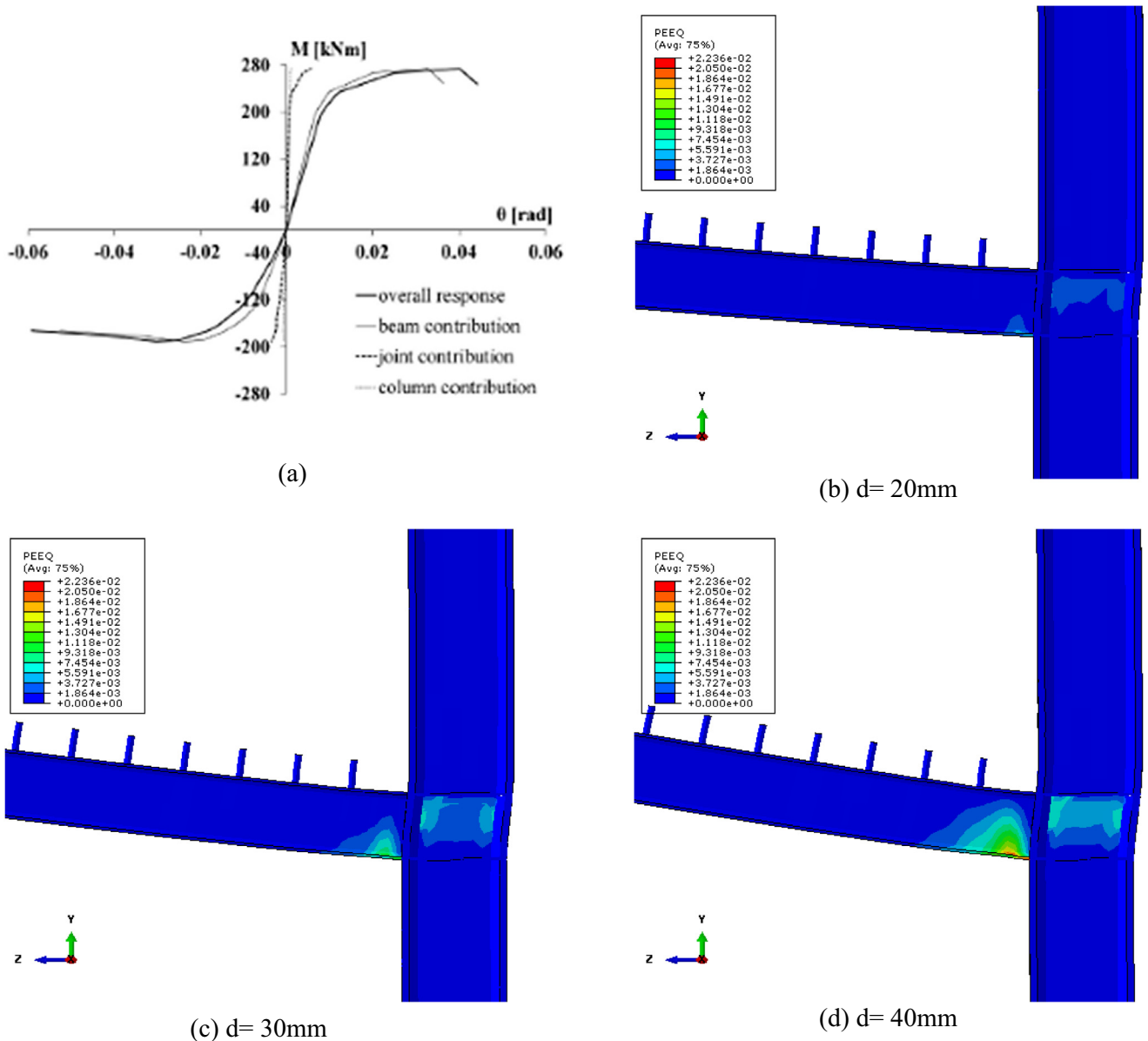


Fig. 19. Analysis of the joint components contributions on the global performance of the WJ specimen. (a) Experimentally derived moment-rotation curves [25] and (b), (c), (d) FE numerically predicted evolution of plastic hinges in the steel components under sagging moment (scale factor = 10).

$$F_{c,slab,Rd} = F_{Rd,1} + F_{Rd,2} \tag{16}$$

The transverse reinforcement area A_T is then determined by imposing translational equilibrium of the beam. In particular, using the notation reported in Fig. 20, the following relations can be written:

$$A_{T,1} \geq \frac{F_{t,1}}{f_{yk}/\gamma_s} = \frac{F_{Rd,1}}{2(f_{yk}/\gamma_s)} \tan \alpha = \frac{F_{Rd,1}}{4(f_{yk}/\gamma_s)} \frac{(b_{eff}^+ - b_b)}{b_{eff}^+} = \frac{F_{Rd,1}}{4(f_{yk}/\gamma_s)} \frac{0,15l - b_b}{0,15l} \tag{17}$$

$$A_{T,2} \geq \frac{F_{Rd,2}}{2(f_{yk}/\gamma_s)} \tag{18}$$

where f_{yk} is the steel characteristic yielding strength, γ_s the steel partial safety factor, α is the angle of spreading of the compressive

stresses, b_{eff}^+ the seismic effective width of the beam under sagging moment, as defined in Eurocode 8, and l the length of the beam.

Although the transverse reinforcement was designed following code prescriptions, during the experimental test the seismic rebars yielded before the complete resistance of the mechanisms was developed, allowing an overall improvement in the ductility of the joint. This occurred mainly due to:

- the over-strength of the concrete with respect to its nominal compressive strength assumed in the design stage;
- the conservative value assumed by Eurocode 8 in defining the resistance of the mechanisms;

In light of this result, the prescriptions of Eurocode 8 on the sizing of the seismic rebar appear to be unsafe. In fact, a ductile design should aim to make the rebars yield before reaching the crushing of struts, making sure that the rebars behaviour governs the overall seismic behaviour of the composite joint. This ductile behaviour

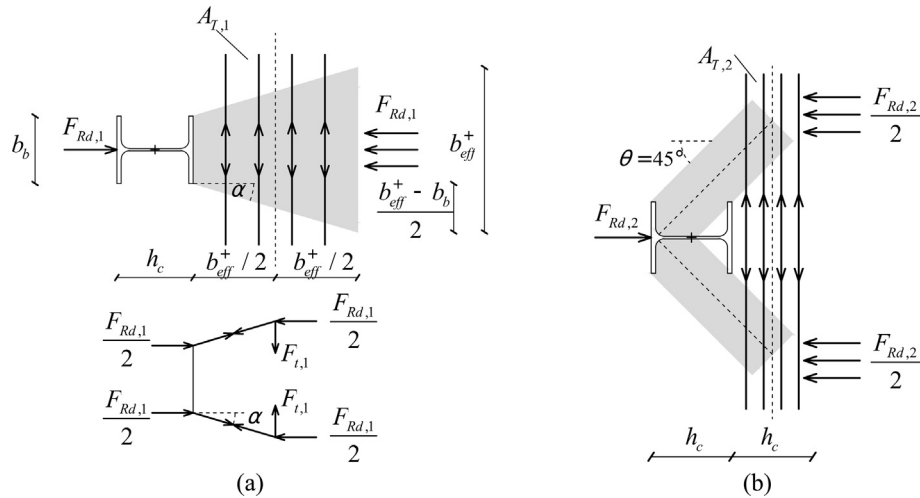


Fig. 20. Strut-and-tie mechanisms in the slab: (a) mechanism 1 and (b) mechanism 2.

could be ensured by calculating the transverse reinforcement area by reversing the sign of inequality in Eqs. (17) and (18) as follows:

$$A_{T,1} \leq \frac{F_{Rd,1}}{2(f_{yk}/\gamma_s)} \tan \alpha \quad (19)$$

$$A_{T,2} \leq \frac{F_{Rd,2}}{2(f_{yk}/\gamma_s)} \quad (20)$$

Therefore, the maximum value of the compressive force transmitted by the slab becomes:

$$F_{c,slab,Rd} = \frac{2A_{T,1}(f_{yk}/\gamma_s)}{\tan \alpha} + 2A_{T,2}(f_{yk}/\gamma_s) \quad (21)$$

Clearly, if the design assumes the beams as dissipative element, the value of Eq. (21) has to satisfy the beam-joint hierarchy (i.e. joint stronger than beam). Conversely, when the dissipation has to be addressed by the joint, the weak element is the joint itself and its ductile behaviour is of paramount importance.

Following these suggestions, at least two positive aspects can be pointed out:

- the calculation of the nominal resistance of the joint will be closer to the actual resistance of the joint in place, given the greater correspondence between the nominal and experimental resistance that characterizes the metal components with respect to the concrete components;
- the collapse will be governed by a ductile component (yielding of the rebars) instead of being governed by a brittle component (crushing of the concrete), allowing a greater absorption of energy and thus a better seismic behaviour.

Moreover, it is worth noting that the area of the transverse rebars $A_{T,1}$ is calculated under the hypothesis that the force $F_{Rd,1}$ transmitted by mechanism 1 spreads along the beam by a length equal to the seismic effective width under sagging moment b_{eff}^+ from the face of the column (Fig. 20), and so the resultant of the transverse tension takes place at a distance of $b_{eff}^+/2$ from the face of the column [41]. Based on this assumption, it seems that the area of the transverse rebars $A_{T,1}$ should depend on the configuration of the joint (b_{eff}^+ changes with the node) and should be spread along a distance equal to b_{eff}^+ from the internal face of the column. However, the Eurocode sets $b_{eff}^+ = 0,15l$ in the calculation of $A_{T,1}$ (see Eq. (17)), regardless of the nodal configuration, and suggests

to spread this transverse reinforcement along a distance equal to b_b from the internal face of the column.

In light of these findings, and since the transversal reinforcement plays a crucial role in the global resistance of a composite joint (above all following the suggested procedure), further studies are hence required to investigate the influence of the transversal rebar sizing, in particular with regards to the angle of spreading α and the length of spreading of the compressive stresses.

6. Summary and conclusions

In this paper, the structural performance of welded steel-concrete joints has been investigated by means of an advanced Finite-Element numerical model (ABAQUS).

Based on a recent research project in which two full-scale tests have been performed to assess the behaviour of exterior composite welded and bolted joints, careful attention has been first paid to the seismic performance of the welded specimen only (WJ). In terms of global measurements and specimen performances, the experiment provided in fact interesting information about the performance of welded joints, i.e.:

- the cyclic behaviour highlighted a general good performance of the WJ joint, in terms of energy dissipation
- the adopted design approach, in line with Eurocode 8 recommendations, was confirmed as a reliable way to guarantee good dissipative behaviour of the composite connection.

The analysis of the experimental local measurements also highlighted some important aspects, i.e.:

- a different participation of the longitudinal rebar due to the shear lag effect;
- the effectiveness of the U-shaped rebar in external composite joints, when subjected to hogging moment;
- the participation of the seismic rebar in the resistance mechanisms, as well as the high ductility performance of the concrete slab in contact with the column edge;
- the analysis of the three FE deformation contributions (i.e. (i) the beam, (ii) column and (iii) column web panel contributions), finally, confirmed that plastic damage was mainly reached in the beam only, while the column highlighted a fully elastic behaviour and the column web panel exhibited only negligible plastic deformations. This finding is in close agreement with the past experimental results.

Based on the experimental test results, a full 3D solid model was then developed in ABAQUS, to further assess the monotonic structural response of the tested welded specimen.

In general, rather close agreement was found between the FE predictions and the corresponding test measurements, both in terms of global and local phenomena. As a result, it is expected that the actual numerical approach could be further extended and implemented for an extensive parametric investigation of composite joints, including a multitude of geometrical and mechanical configurations, as well as composite joints typologies, hence resulting in a valid tool for the calibration of design rules and recommendations.

To this aim, some first considerations were in fact provided for the welded joint object of investigation. As observed from a critical analysis of the experimental and numerical results, in particular, it was noticed that the prescriptions of Eurocode 8 on the seizing of the seismic rebar could present some flaws which could reduce the overall ductility of the joint. On the basis of the developed model, some initial considerations were hence made on the transverse seismic rebars placed in the slab in proximity of the joint.

Acknowledgment

DPC-RELUIS 2015 and 2016 is gratefully acknowledged for funding the research activity.

References

- [1] Leon RT. Analysis and design problems for PR composite frames subjected to seismic loads. *Eng Struct* 1998;20(4–6):364–71.
- [2] Thermou GE, Elnashai AS, Plumier A, Doneux C. Seismic design and performance of composite frames. *J Constr Steel Res* 2004;60:31–57.
- [3] Aribert J, Ciutina A, Dubina D. Seismic response of composite structures including actual behaviour of beam-to-column joints. *Compos Constr Steel Concr* 2006;V:708–17. [http://dx.doi.org/10.1061/40826\(186\)66](http://dx.doi.org/10.1061/40826(186)66).
- [4] Zandonini R. Semi-rigid composite joints. In: Narayanan, editor. *Structural connections stability and strength*, Chapter 3. London (UK): Elsevier Applied Science; 1989. p. 63–120.
- [5] Lee S-J, Lu L-W. Cyclic tests of full-scale composite joint subassemblages. *J Struct Eng* 1989;115(8):1977–98.
- [6] Liew JYR, Teo TH, Shanmugam NE, Yu CH. Testing of steel–concrete composite connections and appraisal of results. *J Constr Steel Res* 2000;56:117–50.
- [7] Bursi OS, Gramola G. Behaviour of composite substructures with full and partial shear connection under quasi-static cyclic and pseudo-dynamic displacements. *Mater Struct/Materiaux et Constructions* 2000;33:154–63.
- [8] Simões R, Simões da Silva L, Cruz P. Experimental behaviour of end-plate beam-to-column composite joints under monotonical loading. *Eng Struct* 2001;23:1383–409.
- [9] Simões R, Simões da Silva L. Cyclic behaviour of end-plate beam-to-column composite joints. *Steel Compos Struct* 2001;1(3):355–76.
- [10] Green TP, Leon RT, Rassati GA. Bidirectional tests on partially restrained, composite beam-to-column connections. *J Struct Eng* 2004;130(2):320–7. Special Issue: Composite and Hybrid Structures.
- [11] Liew JYR, Teo TH, Shanmugam NE. Composite joints subject to reversal of loading—Part 1: experimental study. *J Constr Steel Res* 2004;60:221–46.
- [12] Liew JYR, Teo TH, Shanmugam NE. Composite joints subject to reversal of loading—Part 2: analytical assessment. *J Constr Steel Res* 2004;60:247–68.
- [13] Nakashima M, Matsumiya T, Suita K, Zhou F. Full-scale test of composite frame under large cyclic loading. *J Struct Eng* 2007;133(2):297–304.
- [14] Braconi A, Bursi OS, Fabbrocino G, Salvatore W, Tremblay R. Seismic performance of a 3D full-scale high-ductility steel–concrete composite moment-resisting structure—Part I: design and testing procedure. *Earthquake Eng Struct Dynam* 2008;37:1609–34.
- [15] Vasdravellis G, Valente M, Castiglioni CA. Behavior of exterior partial-strength composite beam-to-column connections: experimental study and numerical simulations. *J Constr Steel Res* 2009;65:23–35.
- [16] Mazzolani FM. Mathematical model for semi-rigid joints under cyclic loads. In: BJORHOVDE R et al., editors. *Connections in steel structures: behaviour, strength and design*. London: Elsevier Applied Science Publishers; 1988. p. 112–20.
- [17] Richard RM, Abbott BJ. Versatile elasto-plastic stress-strain formula. *J Eng Mech* 1975:511–5.
- [18] Salvatore W, Bursi OS, Lucchesi D. Design, testing and analysis of high ductile partial-strength steel–concrete composite beam-to-column joints. *Comput Struct* 2005;83(28–30):2334–52.
- [19] Zhou F, Mosalam KM, Nakashima M. Finite-element analysis of a composite frame under large lateral cyclic loading. *J Struct Eng* 2007;133(7):1018–26.
- [20] Braconi A, Salvatore W, Tremblay R, Bursi OS. Behaviour and modelling of partial-strength beam-to-column composite joints for seismic applications. *Earthquake Eng Struct Dynam* 2007;36:142–61.
- [21] Braconi A, Bursi OS, Fabbrocino G, Salvatore W, Taucer F, Tremblay R. Seismic performance of a 3D full-scale high-ductility steel–concrete composite moment-resisting structure—Part II: test results and analytical validation. *Earthquake Eng Struct Dynam* 2008;37:1635–55.
- [22] Amadio C, Bella M, Bertoni V, Macorini L. Numerical modeling and seismic assessment of steel and steel–concrete composite frames, the line 5 of the RELUIS-DPC 2005–2008 Project. 409–448. Napoli, Italy: Doppiavoce; 2011.
- [23] Eurocode 8. Design provisions for earthquake resistance of structures. Part 1.3: general rules. Specific rules for various materials and elements. Brussels, Belgium: CEN, European Committee for Standardisation; 2004.
- [24] Eurocode 4. Design of composite steel and composite structures. Part 1.1: general rules and rules for buildings. Brussels, Belgium: CEN, European Committee for Standardisation; 2008.
- [25] Pecce M, Rossi F. The experimental behavior and simple modeling of joints in composite MRFs. *Eng Struct* 2015;105:249–63.
- [26] Amadio C, Pecce M, Rossi F, Akkad N, Fasan, M. Experimental study and numerical simulations of composite joints. Proceedings of EUROSTEEL 2014, September 10–12, Naples, Italy, 2014.
- [27] Simulia. ABAQUS theory manual. Dassault Systems; 2012.
- [28] Simulia. ABAQUS analysis manual. Dassault Systems; 2012.
- [29] ATC-24. Guidelines for cyclic seismic testing of components of steel structures for buildings – Report No. ATC-24. Redwood City, CA: Applied Technology Council; 1992.
- [30] Cricri G. Consistent use of the Gurson-Tvergaard damage model for the R-curve calculation, Proceedings of the IGF XX national conference, pp. 138–150, Torino 24–26 June 2009.
- [31] Zhang ZL, Thaulow C, Odegard J. A complete Gurson model approach for ductile fracture. *Eng Fract Mech* 2000;67(2):155–68.
- [32] Jiang W, Li Y, Shu Y, Fan Z. Analysis of metallic ductile fracture by extended Gurson models, Proceedings of 13th international conference on fracture, June 16–21, 2013, Beijing, China; 2013.
- [33] Achouri M, Germain G, Dal Santo P, Saidane D. Implementation and validation of a Gurson damage model modified for shear loading: effect of void growth rate and mesh size on the predicted behavior. *Mater Form ESAFORM* 2012:691–6.
- [34] Kiran R, Khandelwal K. Gurson model parameters for ductile fracture simulation in ASTM A992 steels. *Fatigue Fract Eng Mater Struct* 2013;37(2). <http://dx.doi.org/10.1111/ffe.12097>.
- [35] Jankowiak T, Lodygowski T. Identification of parameters of concrete damage plasticity constitutive model. Foundation of civil and environmental engineering, 6: 53–69. Poznan university of technology, Poland; 2005.
- [36] EN 1992-1-1. Eurocode 2: design of concrete structures: part 1–1: general rules and rules for buildings. Brussels, Belgium: CEN; 2004.
- [37] Birtel V, Mark P. Parameterised finite element modelling of RC beam shear failure. Proceedings of 2006 ABAQUS users' conference, pp. 95–108.
- [38] Cornelissen HAW, Hordijk DA, Reinhardt HW. Experimental determination of crack softening characteristics of normal weight and lightweight concrete. *Heron* 1986;31(2):45–56.
- [39] Qureshi J, Lam D, Ye J. Effect of shear connector spacing and layout on the shear connector capacity in composite beams. *J Constr Steel Res* 2011;67:706–11.
- [40] Bažant ZP. Concrete fracture models: testing and practice. *Eng Fract Mech* 2002;69:165–205.
- [41] Plumier A, Doneux C, Bouwkamp JG, Plumier C. Slab design in connection zone of composite frames. In proc. of the 11th european conference on earthquake engineering. Rotterdam, Holland; 1998.